Korean J. Chem. Eng., 39(6), 1436-1449 (2022)
DOI: 10.1007/s11814-022-1071-x

pISSN: 0256-1115
eISSN: 1975-7220

Temperature nonuniformity management in heat sinks through applying counter-flow design complex minichannels

Morteza Khoshvaght-Aliabadi*,†, Amir Feizabadi, Aida Salimi***, and Mohammad Mehdi Rashidi******

*Department of Chemical Engineering, Shahrood Branch, Islamic Azad University, Shahrood, Iran
**Department of Mechanical Engineering, Faculty of Engineering, Ferdowsi University of Mashhad, Mashhad, Iran
***Department of Mechanical Engineering, West Tehran Branch, Islamic Azad University, Tehran, Iran
****Institute of Fundamental and Frontier Sciences, University of Electronic Science and Technology of China, Chengdu, 610054, Sichuan, P. R. China

(*Received 24 August 2021 • Revised 12 January 2022 • Accepted 17 January 2022*)

Abstract−Thanks to the electronic industrial revolution, miniaturization, which is a trend to manufacture smaller products and devices, has been extended to hardware components. In these devices, the heat flux magnitude increases due to the smaller surface area. Therefore, heat dissipation and temperature uniformity are crucial issues that must be managed precisely, otherwise destructive effects on system performance and device lifespan are unavoidable. Heat sinks are efficient equipment utilized to solve these dire consequences. In this study, to improve the temperature uniformity of electronic components, novel minichannels, including straight walls with wavy fins (SWS) and wavy walls with straight fins (WSW), were examined with counter-flow patterns. The observations imply that these novel minichannels bring 18.1-40.3% decrease of the base temperature under the heat flux of 100 kW m^{-2}. It is also revealed that using the novel minichannels can increase the temperature uniformity up to 93.1%. In addition, overall hydrothermal performance can be enhanced as high as 1.64 under the pumping power of 0.0374 W. It was also found that the use of WSW models leads to lower magnitudes of pumping power compared to SWS models. It is concluded that applying the proposed minichannels could be an efficient approach to manage temperature non-uniformity in heat sinks.

Keywords: Heat Sink, Temperature Uniformity, Counter-flow, Maximum Base Temperature Difference

INTRODUCTION

One of the most critical problems with heat removal techniques in high heat flux cases is temperature non-uniformity, which mainly originates from two factors: rising temperature along stream-wise direction and hotspots. Consequently, creating undesirable thermal stresses may be associated with detrimental effects on the efficiency and lifespan of electronic devices [1]. Hence, it is necessary to improve cooling devices to mitigate the temperature non-uniformity.

To achieve desired heat removal goals in heat sinks, several innovative passive approaches have been reported, such as using interruption and re-development of boundary layers by surface roughness [2], pin-fins [3,4], and ribs [5-7]. In addition, the novel structures of sinusoidal geometry [8-11], as well as the periodic expansion-constriction cross-section [12-14] have been widely utilized in heat sinks. Generally, most published works have emphasized hydrothermal features of heat sinks, particularly the Nusselt number and friction factor, while available literature focusing on the temperature non-uniformity in heat sinks is scarce.

A non-uniform heat sink with non-uniform fin density was considered by Rubio-Jimenez et al. [15,16]. They studied the effects of fin geometry (circle, square, elliptical, and flat) and their arrangements on thermal characteristics through a numerical approach. The studied cases, particularly the flat-shaped model, had better temperature uniformity compared to other schemes. Similarly, Vilarrubí et al. [17] proposed a new configuration of the heat sink, considering variable fin density microchannels along the stream-wise direction. A comparative analysis of the gradient and uniform temperature distribution was done by Feng et al. [18-20] to evaluate temperature uniformity. They concluded that the gradient distribution design could effectively improve temperature uniformity. Lorenzini-Gutierrez and Kandlikar [21] studied the effectiveness of establishing temperature uniformity by using variable fin density. Their results revealed that the maximum temperature difference of the most efficient configuration was less than 30 K in comparison with the temperature difference of 38 K (for continuous fins) and 51 K (for smooth flow channel configurations). Gonzalez-Hernandez et al. [22] numerically investigated the performance of various minichannels consisting of offset-strip fins with different fin densities. It was found that making an effective modification in heat sink design leads to mitigating temperature non-uniformity and keeping the surface temperature of IC chips at a reasonable operating level. Li et al. [23] introduced four different microchannel configurations, considering shark skin bionic structures as ribs to improve thermal performance and they concluded that, compared to the traditional minichannel heat sinks, the temperature non-uniformity diminished noticeably.

Water-cooled heat sinks consist of several parallel minichannels, in which the working fluid flows in a single direction. Consequently, the temperature experiences a sharp rise along the flow direction,

†To whom correspondence should be addressed.
E-mail: mkhaliabadi@gmail.com, mkhaliabadi@iau-shahrood.ac.ir
Copyright by The Korean Institute of Chemical Engineers.

resulting in non-uniformity in temperature distribution. Most of the studies reviewed here have focused on the geometrical modification of minichannel heat sinks, using variable fin density to enhance temperature uniformity. However, to the authors' best knowledge, there have been scarce investigations into comparing counter and parallel flow patterns in minichannel heat sinks. The only researchers who investigated the influence of both parallel and counter-flow arrangements of the double-layer minichannel heat sinks on temperature non-uniformity were Leng et al. [24]. Hence, in the present contribution, the idea of interrupting straight and wavy minichannel heat sinks is numerically examined, and the effects of flow arrangements on the development of swirl flows and chaotic advection of boundary layers are investigated as well.

PROBLEM DESCRIPTION

When a liquid-cooled heat sink is used as cooling technique for modern microprocessors, it is necessary to determine the temperature distribution, because non-uniform temperature distribution is a problematic issue in heat sinks. In this study, the counter-flow design in novel complex minichannels is suggested to overcome the problem of surface temperature non-uniformity. Schematics of studied cases are displayed in Fig. 1. Two groups of the complex minichannels, including straight walls with wavy fins (SWS) and wavy walls with straight fins (WSW) are considered. As shown in this figure, the wavy structure has a non-uniform pattern with low-to-high or high-to-low configurations. Application of wavy structure

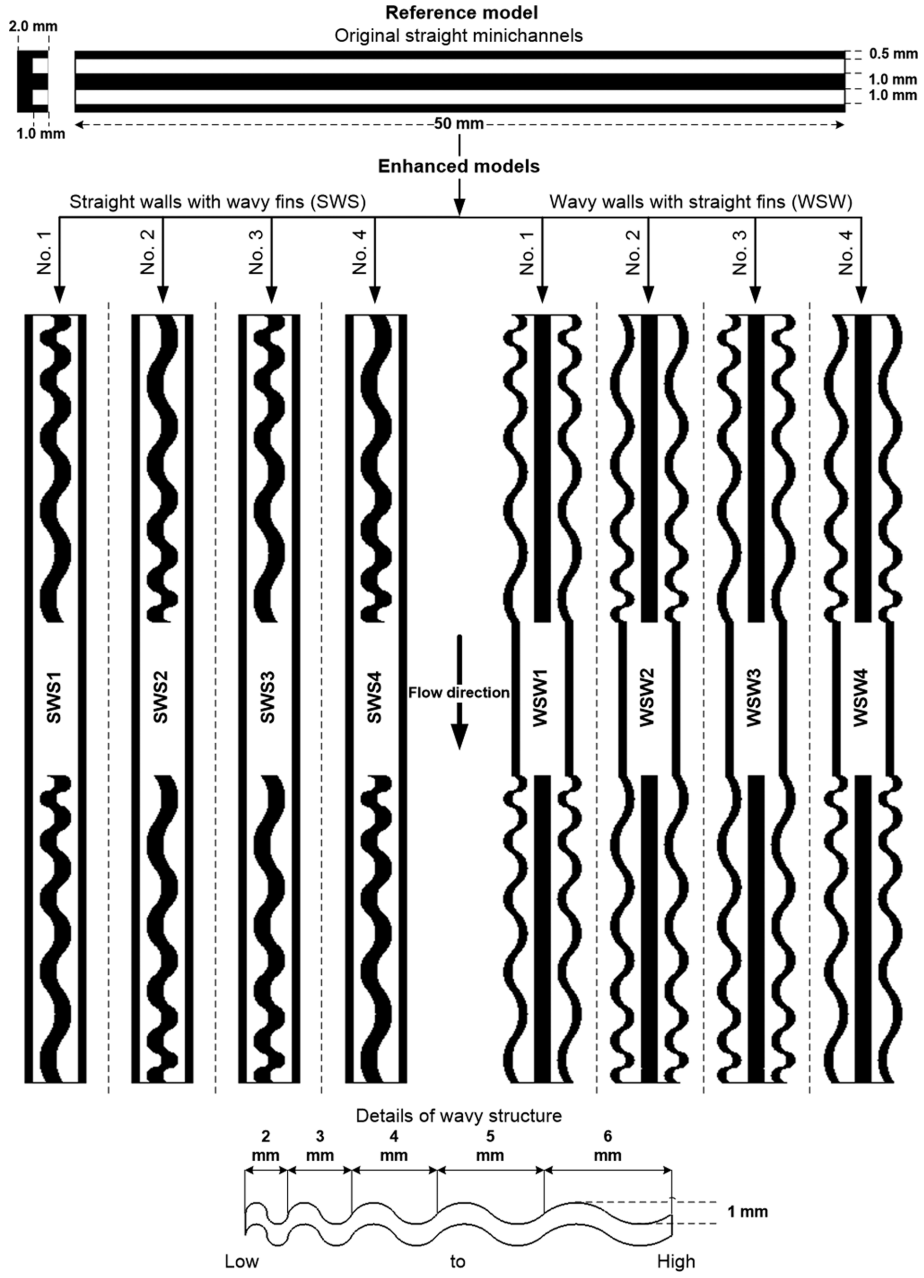


Fig. 1. Physical structure of studied models.

with non-uniform wave-lengths was suggested by Ref. [25]. As a matter of fact, such designs result in local increases in heat transfer coefficient and may contribute to temperature uniformity. All enhanced models have the same overall dimensions. In the reference model, the length, width, and depth of minichannels are 50, 1, and 1 mm, respectively, and the thickness of walls and fins are 0.5 and 1.0 mm, respectively. In all models, the height of the base material is 1.0 mm. At the bottom of Fig. 1, details of the wavy structure are also defined, in which the wave amplitude is constant and equal to 1 mm, but the wavelength varies from 2 mm to 6 mm. As presented in this figure, some abbreviations are used to facilitate the interpretation of results analysis. Synoptically, in the present work, a numerical analysis is carried out for the introduced models exposed to a uniform heat flux of 100 kW m^{-2}. An experimental study is also done to obtain the required data for the validation study. In the next section, details of the implementation techniques are presented.

IMPLEMENTATION

1. Numerical Simulation

Fig. 2 outlines samples of the computational domain for both co-flow and counter-flow patterns. They have similar dimensions and footprints (4×50 mm^2). To shorten running times the computational domain is a part of an actual heat sink, which is examined experimentally, and it will be further explained in the following subsection. Other simplifying assumptions are as follows: (i) steady-state condition for all parameters, (ii) Newtonian, incompressible, and single-phase for coolant, (iii) continuum and laminar for flow, (iv) constant and uniform value for heat flux, (v) neglectable values for viscous dissipation, gravitational force, natural and radiation mechanisms. By applying the mentioned assumptions, the conservation equations will be employed in the following forms:

- Continuity

$$\frac{\partial v_x}{\partial x}+\frac{\partial v_y}{\partial y}+\frac{\partial v_z}{\partial z}=0 \tag{1}$$

- Momentum

$$v_x\frac{\partial v_x}{\partial x}+v_y\frac{\partial v_x}{\partial y}+v_z\frac{\partial v_x}{\partial z}=-\frac{1}{\rho}\frac{\partial p}{\partial x}+\frac{\mu}{\rho}\left[\frac{\partial^2 v_x}{\partial x^2}+\frac{\partial^2 v_x}{\partial y^2}+\frac{\partial^2 v_x}{\partial z^2}\right] \tag{2}$$

$$v_x\frac{\partial v_y}{\partial x}+v_y\frac{\partial v_y}{\partial y}+v_z\frac{\partial v_y}{\partial z}=-\frac{1}{\rho}\frac{\partial p}{\partial y}+\frac{\mu}{\rho}\left[\frac{\partial^2 v_y}{\partial x^2}+\frac{\partial^2 v_y}{\partial y^2}+\frac{\partial^2 v_y}{\partial z^2}\right] \tag{3}$$

$$v_x\frac{\partial v_z}{\partial x}+v_y\frac{\partial v_z}{\partial y}+v_z\frac{\partial v_z}{\partial z}=-\frac{1}{\rho}\frac{\partial p}{\partial z}+\frac{\mu}{\rho}\left[\frac{\partial^2 v_z}{\partial x^2}+\frac{\partial^2 v_z}{\partial y^2}+\frac{\partial^2 v_z}{\partial z^2}\right] \tag{4}$$

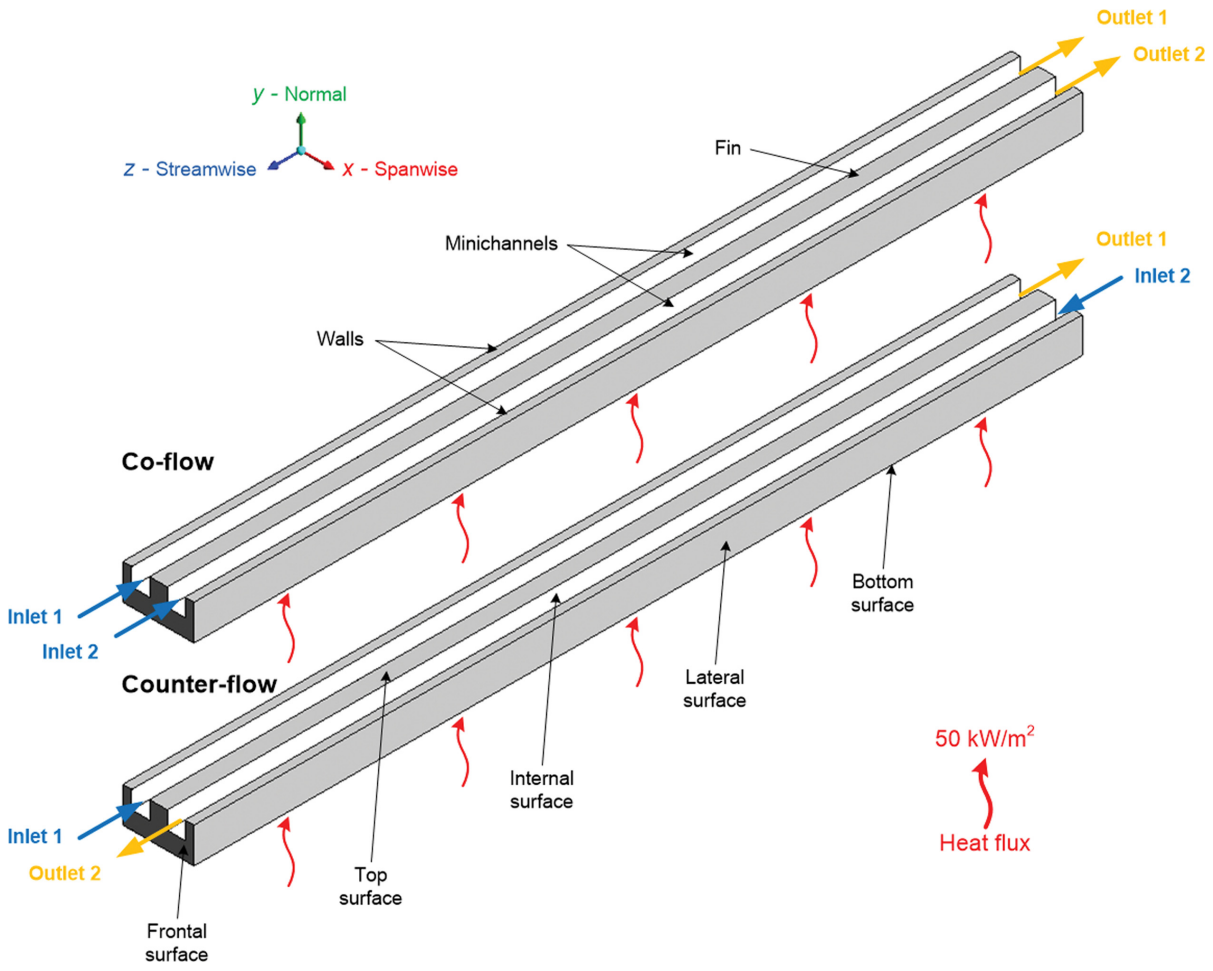


Fig. 2. Sample of computational domain.

Table 1. Mathematical definition of boundary conditions

Surface name	Boundary condition
Inlet	$w = w_{in} = \text{const}$, $u = w = 0$, $T_f = T_{in} = \text{const}$
Outlet	$\frac{\partial u}{\partial z} = \frac{\partial v}{\partial z} = \frac{\partial w}{\partial z} = 0$, $\frac{\partial T_f}{\partial z} = 0$
Bottom	$u = v = w = 0$, $-k_s \frac{\partial T}{\partial y} = q$
Lateral	$\frac{\partial v}{\partial x} = \frac{\partial w}{\partial x} = u = 0$, $k_s \frac{\partial T}{\partial x} = 0$
Internal	$u = v = w = 0$, $T_f = T_s$, $-k_f \frac{\partial T_f}{\partial n} = -k_s \frac{\partial T_s}{\partial n}$
Others	$u = v = w = 0$, $\frac{\partial T}{\partial x} = \frac{\partial T}{\partial y} = \frac{\partial T}{\partial z} = 0$

- Energy (Fluid)

$$v_x \frac{\partial T}{\partial x} + v_y \frac{\partial T}{\partial y} + v_z \frac{\partial T}{\partial z} = \frac{k}{\rho c_p}\left[\frac{\partial^2 T}{\partial x^2} + \frac{\partial^2 T}{\partial y^2} + \frac{\partial^2 T}{\partial z^2}\right] \quad (5)$$

where v_x, v_y, and v_z denote the velocity components along the span-wise, normal, and stream-wise directions, respectively. Also, p and T indicate the fluid pressure and temperature, respectively, ρ, μ, k, and c_p are the thermophysical properties of the fluid.

- Energy (Solid)

$$0 = k_s\left[\frac{\partial^2 T_s}{\partial x^2} + \frac{\partial^2 T_s}{\partial y^2} + \frac{\partial^2 T_s}{\partial z^2}\right] \quad (6)$$

where T_s is the solid temperature and k_s is the thermal conductively of the solid.

According to the computational domain shown in Fig. 2, uniform velocity and constant temperature are adopted on the model's entrance. Also, at the exit of the computational domains, the pressure outlet condition is adopted. The no-slip and adiabatic-wall conditions are characterized for the lateral surfaces except for the bottom surface, which is subjected to a constant heat flux. Meanwhile, the interfaces between the water and heat sink are set as coupled walls. Mathematical details about the prescribed boundary conditions are presented in Table 1.

Table 2. Physical properties of materials

Material	ρ (kg·m^{-3})	c_p (J·kg^{-1}·K^{-1})	μ (Ps·s)	k (W·m^{-1}·K^{-1})
Water	998.2	4,182	0.001003	0.6
Aluminum	2,719	871	------	202.4

Note that Aluminum material was used for the solid domain, while water was adopted as heat transfer agent to remove the heat load, due to its high heat capability. The physical properties of materials used in the CFD simulations were assumed to be constant and are listed in Table 2.

The Green-Gauss cell-based method was chosen for the transport quantity gradients in all presented cases. In terms of solver settings, the second-order upwind scheme is utilized for the pressure, momentum, and energy equations. In addition, the coupling of pressure and velocity is done by the SIMPLE algorithm. In the current simulations, it is supposed that the convergence is achieved when the residual of each equation is lower than 10^{-5} for the continuity equation, 10^{-6} for the momentum equation, and 10^{-8} for the energy equation. Details of this analysis are presented in Table 3 for the reference model at the maximum Reynolds number, and the temperature and pressure differences between the inlet and the outlet are obtained through simulations.

To find the best pattern of grids, which corresponds to precise numerical results and minimal computational times, a detailed analysis was carried out. As shown in Fig. 3, sufficiently finer grids are used at the common boundaries between solid and fluid domains. A sequential grid independence study is kept doing till the error percentage for thermal and hydraulic parameters does not exceed ±0.5%. Therefore, to determine the influence of the number of grids on the obtained results, various sets were studied at the highest Reynolds number (i.e., 900). For instance, for the straight model, the considered sets are (100-30-250), (125-40-300), (150-50-350), and (175-60-350), where the first two numbers refer to the heat sink sides and the third number refers to the heat sink length. The dimensionless parameters of Nusselt number and friction factor are considered as criteria for distinction. As displayed in Table 4, results reveal that the variations of the Nusselt number and fric-

Table 3. Effect of convergence criteria on numerical results

Set no.	Convergence criteria values	$\Delta T = T_{out} - T_{in}$	T_{i+1} & T_i deviation	$\Delta P = P_{out} - P_{in}$	P_{i+1} & P_i deviation
1	10^{-3} for continuity 10^{-4} for momentum 10^{-8} for energy	2.73	-----	1,879.85	-----
2	10^{-4} for continuity 10^{-5} for momentum 10^{-8} for energy	2.67	2.2	1,893.29	0.71
3	10^{-5} for continuity 10^{-6} for momentum 10^{-8} for energy	2.65	0.75	1,902.23	0.47
4	10^{-6} for continuity 10^{-6} for momentum 10^{-8} for energy	2.66	0.37	1,906.41	0.22

Table 4. Results of grid independence test

Grid no. in *x*-direction	Grid no. in *y*-direction	Grid no. in *z*-direction	Average Nu number	Nu_{i+1} & Nu_i deviation	Average f factor	f_{i+1} & f_i deviation
100	30	250	23.26	-----	0.416	-----
125	40	300	22.67	2.53	0.421	1.20
150	50	350	22.31	1.58	0.424	0.71
175	60	350	22.16	0.67	0.426	0.47

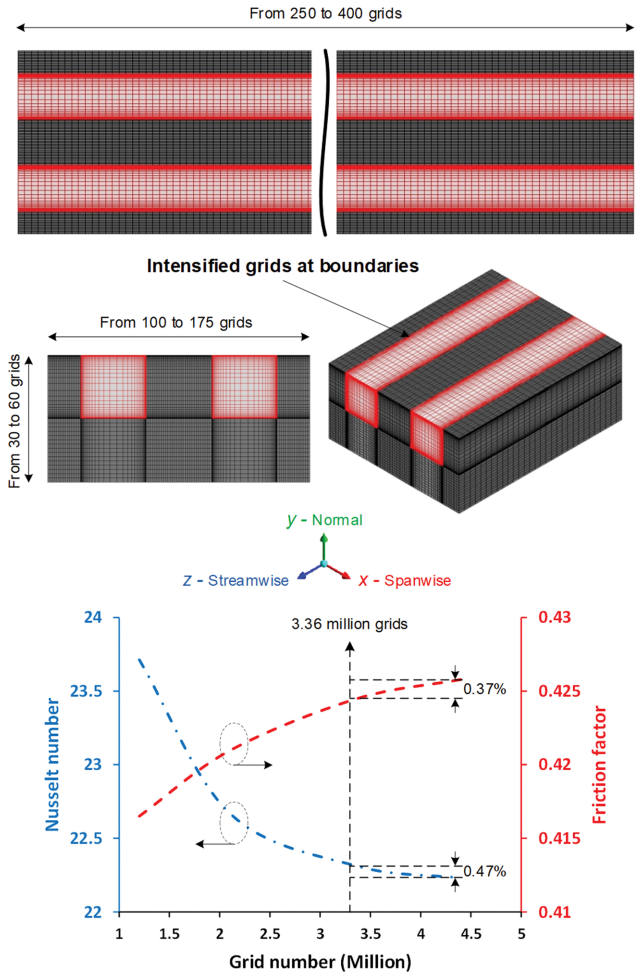


Fig. 3. Details of grid independence study.

tion factor are negligible (less than 0.5%) for the grid with 150, 50, and 350 nodes in the x, y, and z directions, respectively. Moreover, the percentage difference of Nusselt number and friction factor between coarsest and finest grid levels is lower than 5%. So, a quantitative analysis of the numerical uncertainties is unnecessary.

2. Experimental Study

To implement the procedure required for the verification of the numerical models by empirical data, an experimental study was also carried out. The testing model was an actual model with straight minichannels, as shown in Fig. 4(a). It was fabricated from an aluminum block with a length of 170 mm, a width of 40 mm, and a height of 5 mm. Two plenums were designed at both sides to establish a uniform coolant distribution through the minichannels. The depths of these sections are the same as minichannels, and their length and width are 20 mm. The heat sink is connected to a prefabricated plexiglass cube, which is filled with a copper block. The copper block symbolizes an electromechanical device, in which heat is produced by a cylindrical heater. As shown, a 10 mm diameter hole is drilled in the copper block to embed the cartridge heater. Then, the assembled test module is connected to the test setup. Fig. 4(b) displays a schematic diagram of the setup, on which the experiments are done. Both sides of the test module are attached to the measuring equipment by suitable connections. On each side, a T-type thermocouple and digital pressure transmitter are applied to measure the temperature and pressure, respectively. Also, four K-type thermocouples are employed to evaluate the base temperature. These sensors are placed inside the holes embedded in the side surface area of the heat sink. An AC power source supplies an alternating electrical current for the cartridge heater with the help of a variac transformer. The current and voltage for the studied input power (100 W) are justified by a multifunction metering device. The outlet of the test module is connected to a mass measurement system, by which the flow rate of the water is evaluated. Note that, the water flow inside the test module is produced by a centrifugal pump, which is installed at the beginning of the loop. Finally, the temperature of the water is restored by using the cooling unit.

DATA REDUCTION

To obtain the required data for the validation, first, the thermal and hydraulic performances were evaluated in terms of non-dimensional parameters, i.e., Nusselt number and friction factor versus Reynolds number. These non-dimensional parameters are estimated as follows:

$$Nu = \frac{hD_h}{k} \tag{7}$$

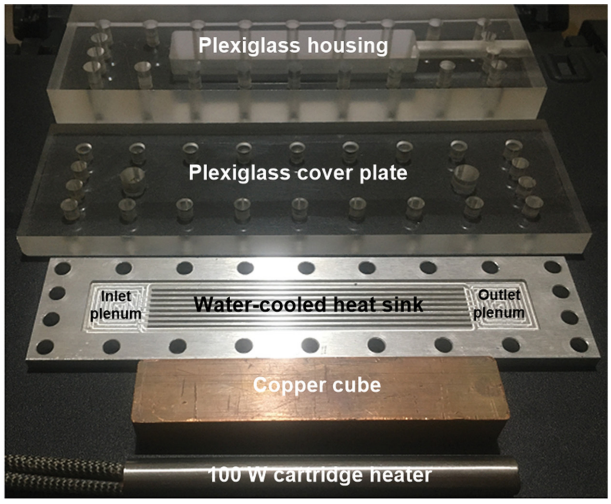
In the above equation (Nusselt number), D_h is the hydraulic diameter of the minichannels,

$$D_h = \frac{4A_c l}{A_t} \tag{8}$$

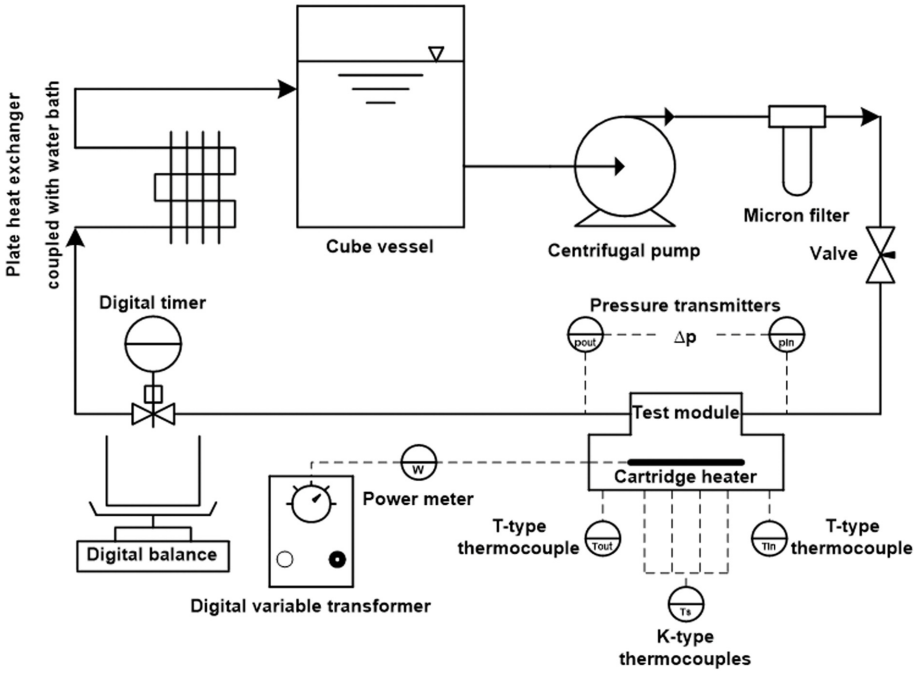
where A_c, A_t, and l indicate the frontal surface area, wetted surface area, and length of the minichannels, respectively.

Also, k is the thermal conductivity of the coolant, and h is the dimensional heat transfer coefficient,

$$h = \frac{mc_p(T_{out} - T_{in})}{A_t(T_s - (T_{in} + T_{out})/2)} \tag{9}$$



(a)



(b)

Fig. 4. (a) Test module (b) Setup.

where m is the mass flow rate, c_p is the specific heat capacity of the coolant, and T_{in}, T_{out}, and T_s are the inlet, outlet, and surface temperatures, respectively.

$$f = \frac{2\Delta p D_h}{l \rho u_{in}^2} \tag{10}$$

In the above equation (Darcy friction factor), Δp is the pressure loss, ρ is the density of the coolant, and u_{in} is the inlet velocity.

$$Re = \frac{\rho u_{in} D_h}{\mu} \tag{11}$$

In the above equation (Reynolds number), μ is the dynamic viscosity of the coolant.

The average base temperature and the maximum base temperature difference are also studied:

$$T_{b,\,avg.} = \frac{\int T_b dA}{\int dA} \tag{12}$$

$$\Delta T_{b,\,max.} = T_{b,\,max} - T_{b,\,min} \tag{13}$$

where $T_{b,max.}$ and $T_{b,min.}$ are, respectively, the maximum and minimum temperatures in the base surface.

Moreover, the most remarkable feature of the novel designs is their ability to reduce the maximum base temperature of the heat sink. Thus, a non-dimensional parameter is defined to indicate the temperature uniformity [26],

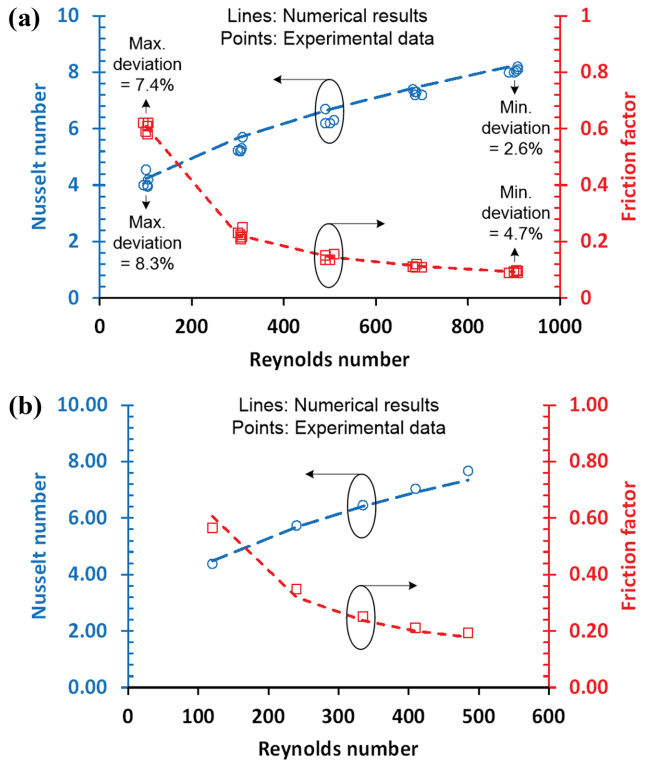


Fig. 5. Validation of numerical results (a) Co-flow design (b) Counter-flow design.

$$\theta=\left[1-\frac{\Delta T_{b,max.}}{T_{b,avg.}}\right]\times 100 \tag{14}$$

Further, a thermal performance index is considered to assess the performance of the novel minichannels, which considers the heat transfer and friction effects simultaneously. This term is the ratio of the heat transfer enhancement to rise of pressure drop as below [27]:

$$\eta=\frac{(Nu_{movel}/Nu_{straight})}{(f_{novel}/f_{straight})^{1/3}} \tag{15}$$

RESULTS AND DISCUSSION

1. Validation

To confirm the validity of the reported findings, a two-step validation study was performed. In the first step, the results obtained from the numerical simulation are compared to the data recorded from the experimental study. As shown in Fig. 5(a), there is a good agreement between the experimental data and the numerical results. Note that the experimental tests are repeated several times for each Re, and five centralized points are chosen and provided in this figure. One can see that the deviations of both Nusselt number (Nu) and friction factor (f) are larger at the smaller values of Re. Higher heat loss from the test module and lower accuracy of pressure transmitters at the smaller Re can be the main reasons for these deviations. However, the maximum absolute deviations of 8.3% and 7.4% are observed for Nu and f, respectively.

To further investigate the reliability of the current results, an additional numerical simulation was conducted, as the second step of the validation study. In this step, the case, which was studied experimentally by Tikadar et al. [28], is considered as the reference model. They conducted the experiments for a specific range of Re (from 120 to 485), due to the limited pump capacity. Actually, the current comparison is presented to verify the results obtained for the counter-flow design. As displayed in Fig. 5(b), our numerical simulations can satisfactorily confirm their experimental data. The maximum absolute deviations of Nu and f are 4.2% and 8.1%, respectively. These results indicate that the present CFD model can be employed successfully to study flow and temperature distributions of heat sinks.

2. Thermal Characteristics

The alterations of the average base temperature ($T_{b,avg.}$) as a function of the coolant inlet velocity (u_{in}) are shown in Fig. 6. Obviously, $T_{b,avg.}$ decreases by increasing u_{in}, meaning that the coolant with a larger velocity can reduce the thermal resistances because of its better heat transfer ability. Indeed, increasing u_{in} affects the flow features and pathlines inside the minichannels. Complex flow features can be found in such novel geometries, particularly in the middle part, with counter-flow design. For instance, analyzing the flow pathlines in WSW3 and the corresponding temperature con-

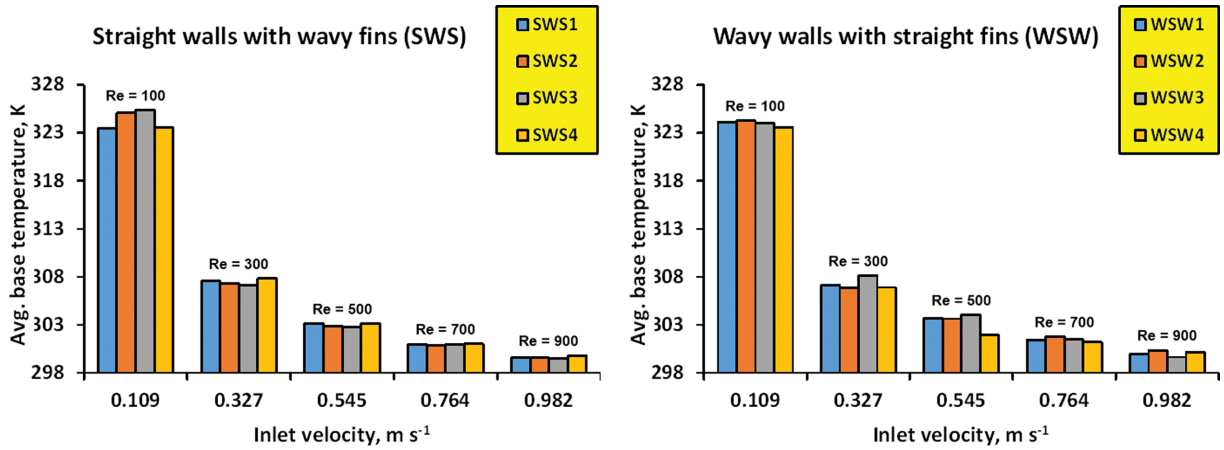


Fig. 6. Average base temperature vs. Inlet velocity.

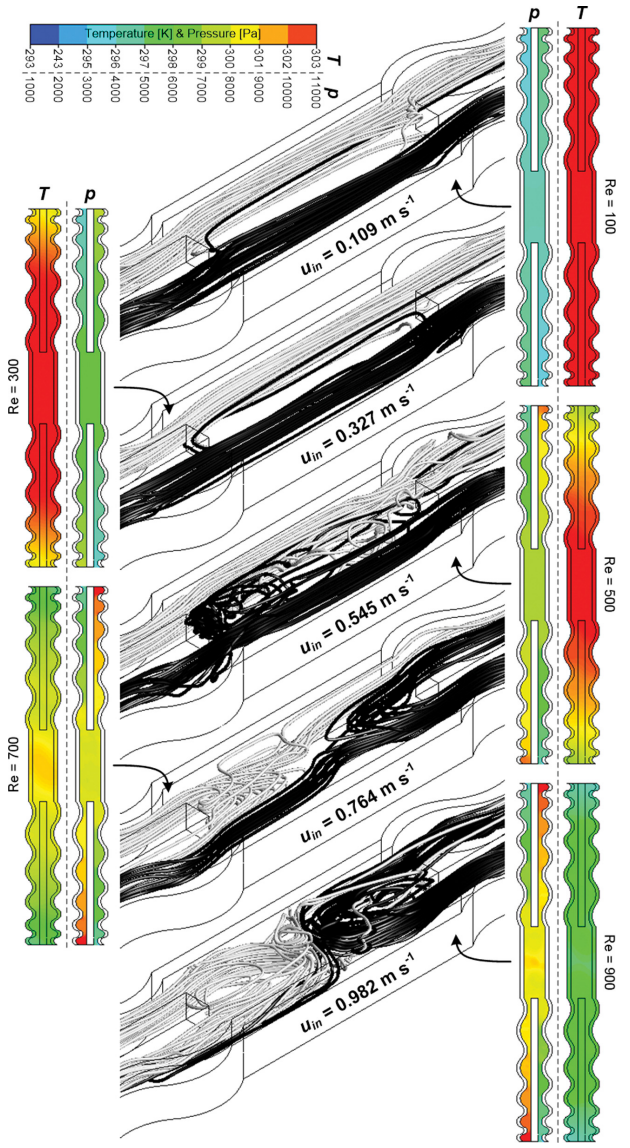


Fig. 7. Effects of inlet velocity on pathlines, temperature distribution on base surface, and pressure distribution on certain plane of y=1.5 mm inside WSW3.

tours discloses that larger values of u_{in} generate more complex pathlines leading to lower $T_{b,avg}$. To find the effects of u_{in} on $T_{b,avg}$, understanding the impact of u_{in} on the pressure distributions is also helpful. As shown in Fig. 7, when u_{in} is low (Re=100 or 300), the pathlines are parallel and they continue to move in a straight line, and after the middle part, they enter the opposite minichannel. Therefore, there is no noticeable pressure difference across the middle part, and Bernoulli's effects are negligible without the formation of rotational flows. However, with increasing u_{in} (Re ranges from 300 to 500), the pressure difference across the middle part goes up because of the stronger reciprocating flow. This leads to some rotational flows through the middle part. With further increase in u_{in} (Re ranged from 500 to 700), an interesting phenomenon occurs and a portion of the inlet coolant coming from each side to the middle part merges with the inlet coolant coming from the opposite minichannel and moves in the opposite direction. It can be accountable for the break-up of boundary layers and reduction of $T_{b,avg}$. At the maximum u_{in} (Re=900), the flow pattern changes completely, so that almost all the inlet coolant coming from each side rotates 180 degrees and enters the adjacent minichannel. As a result, complex and rotational flows occur in the middle part. Meanwhile, the variation of pressure at the intersection of these flows is evident in the pressure contours. The mentioned mechanisms have positive effects on the thermal performance, leading to lower $T_{b,avg}$ at larger u_{in}.

It is also revealed that the alteration of the maximum base temperature difference ($\Delta T_{b,max}$) depends on u_{in}. Fig. 8 is plotted to elucidate the variation of $\Delta T_{b,max}$ versus u_{in}. As the figure represents, $\Delta T_{b,max}$ generally decreases with increasing u_{in}. It means that the thermal performance is improved. However, there are exceptions to the trend as well. For instance, although regarding Fig. 6, in SWS4 $T_{b,avg}$ at u_{in}=0.982 m s^{-1} is lower than that at u_{in}=0.545 m s^{-1}, $\Delta T_{b,max}$ of this model at both u_{in}=0.982 m s^{-1} and u_{in}=0.545 m s^{-1} is almost the same. The highest reductions in $\Delta T_{b,max}$ reach 1.98 K and 1.86 K for SWS4 and WSW4 at u_{in}=0.982 m s^{-1} (Re=900).

To clarify why a gap is considered in the middle part of the models, the temperature contours of the coolant at the maximum u_{in} (Re=900) for different models are provided in Fig. 9(a). It is found that in the reference model, the coolant temperature is gradually

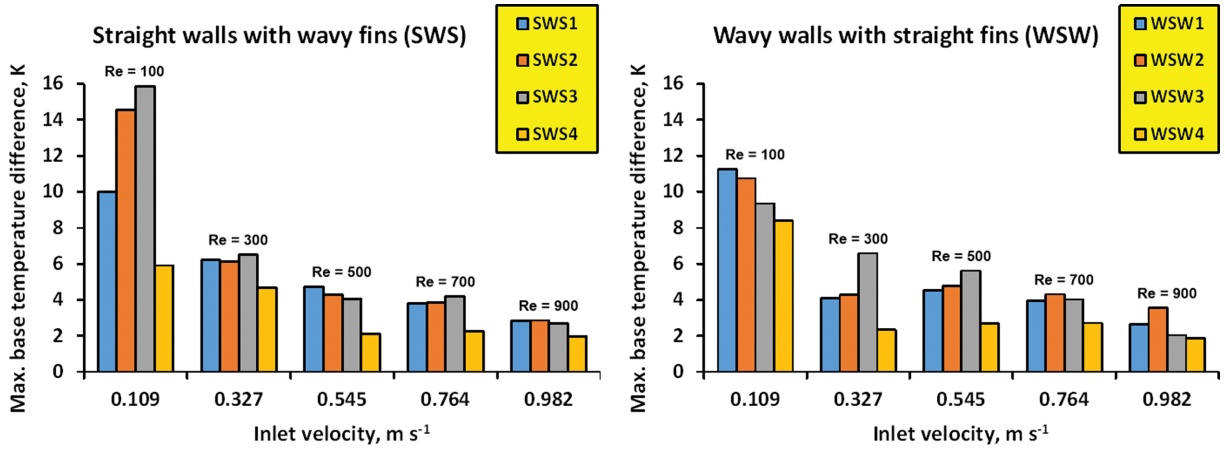
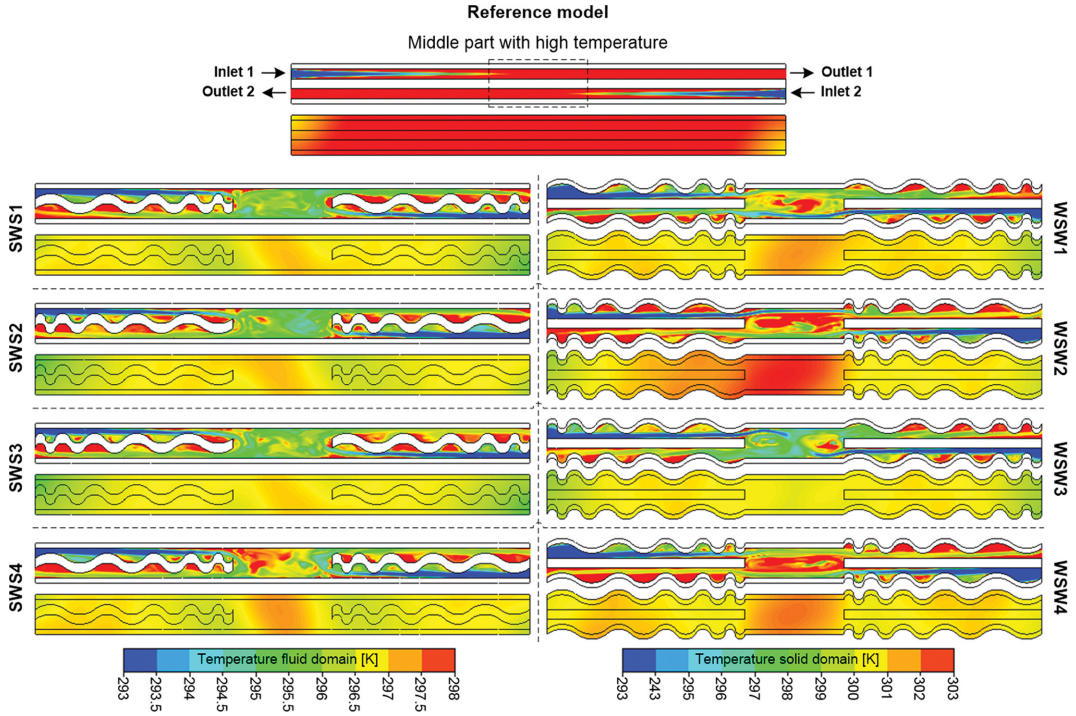
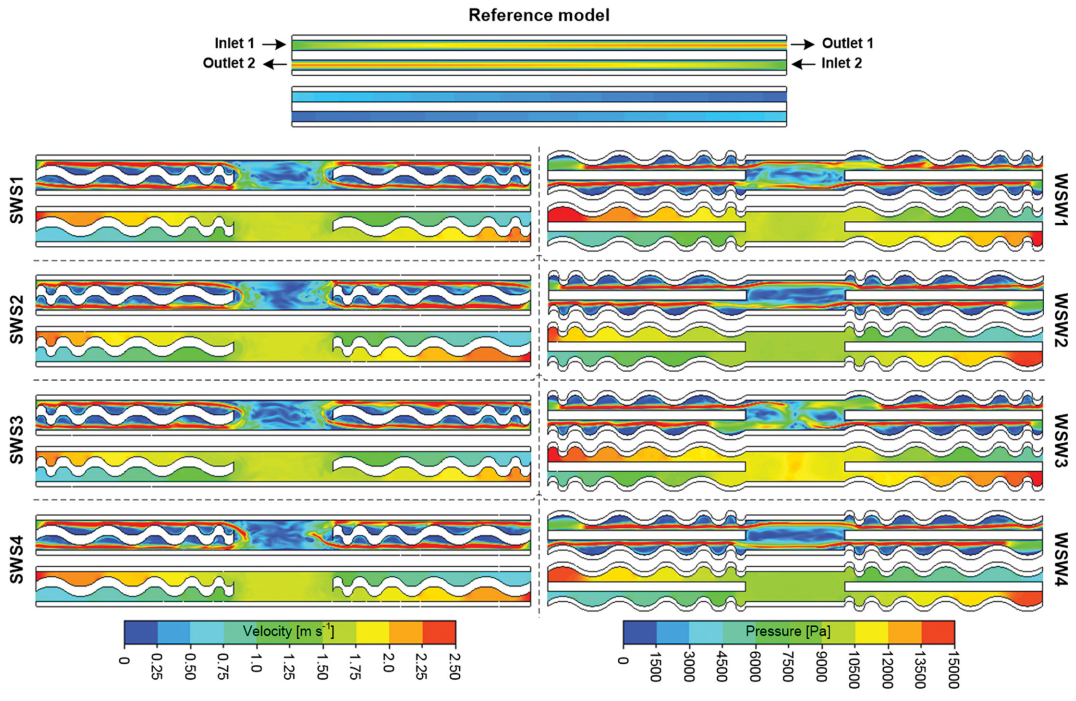


Fig. 8. Maximum base temperature difference vs. Inlet velocity.



(a)



(b)

Fig. 9. (a) Temperature distributions on a certain plane of y=1.5 mm (top) and base surface (bottom) at Re=900 (b) Velocity (top) and pressure (bottom) distributions on a certain plane of y=1.5 mm at Re=900.

rising through the straight minichannels, and the thermal boundary layers are growing. Regarding this figure, due to the opposite flow in the adjacent minichannels, the maximum thermal resistance is expected in the middle part, leading to a higher temperature in this section. Therefore, creating an empty space in the middle part can lead to significant changes. The results display that the geometries of both the walls and the fins affect the flow features and heat transfer inside the middle part. As the figure shows, applying WSW3 results in lower values of the coolant temperature in the middle part. In addition to lower coolant temperature, the base

surface temperature becomes more uniform in this model, which implies that this model has greater thermal performance. Details of fluid flow and pathlines corresponding to WSW3 are presented in Fig. 7. The thermal performance of this model profoundly improves with increasing Re. Regarding Fig. 7, the lower coolant temperature and base surface in the middle part, which emanates from higher pathlines perturbations, leading to much better cooling performance.

3. Hydraulic Specifications

Another important point is the hydraulic specifications of the considered models. The main mechanisms that affect the hydraulic specifications of the novel minichannels are two factors: (1) flow blockages triggered by wavy walls and fins, and (2) flow irregularities generated by swirl flows. Regarding Fig. 1, by combining straight structure and wavy structure, the flow surface area in the novel minichannels is changed by ±50% (from 0.5 to 1.5 mm^2) compared to the conventional minichannel, which has a flow surface area of 1 mm^2. Hence, severe expansion and contraction appear, resulting in large flow blockages and pressure losses. The pressure loss principally stems from velocity and pressure alterations, so the distributions of these parameters must be studied comprehensively, as shown in Fig. 9(b). To visualize the impacts of various patterns of wavy walls and fins, the alterations of velocity and pressure are presented on a certain plane (y=1.5 mm) at Re=900. The velocity contours illustrate that the maximum value appears at the smallest flow surface area, where the pressure contours experience reductions as a result of Bernoulli effects. It can be seen that in all the models, when the coolant flows in the integral sections (minichannels), the pressure decreases gradually along the stream-wise direction, and variations can only be seen before and after expansions and contractions. This pressure difference between these sections generates some swirl flows in the corrugations. The details of the formation process of these flows have been discussed in previous studies [29,30], so will not be discussed here.

However, it can be explained that, since all the models have the same number of corrugations, the pressure loss caused by wall shear stress is almost the same. This shear stress is generated by the wavy walls and fins and the main reason for the difference is the gener-

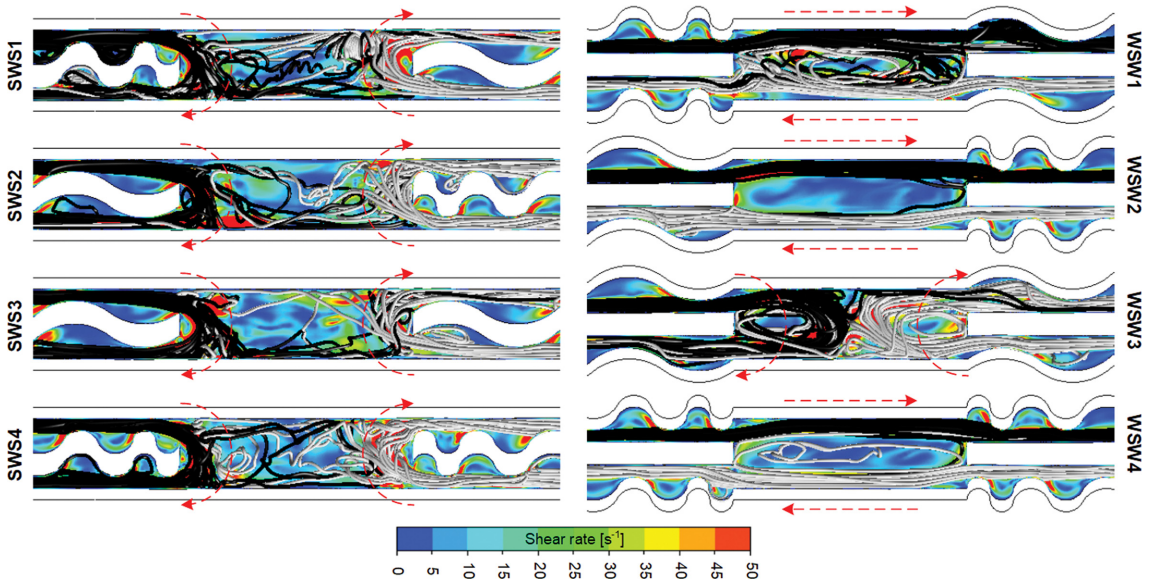


Fig. 10. Pathlines and shear rate distributions on internal surface at Re=900.

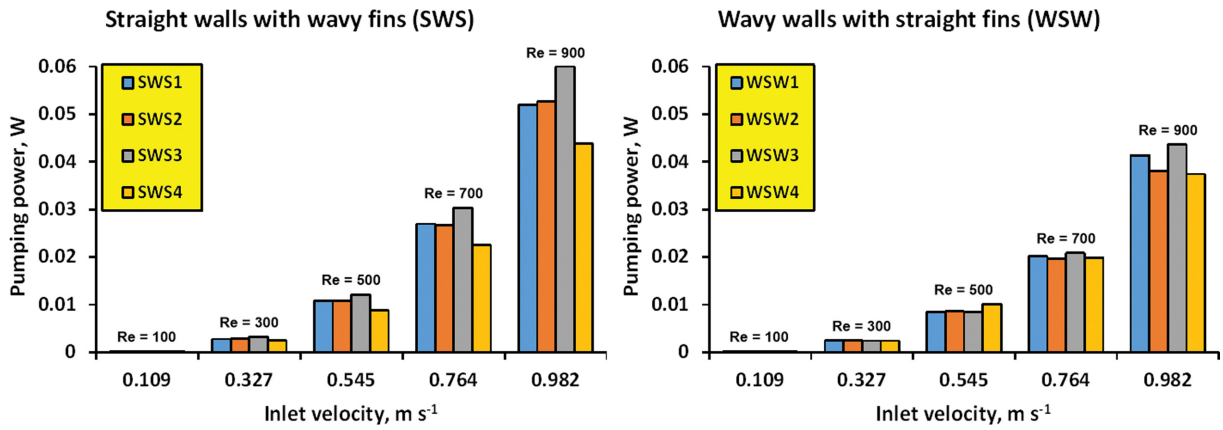


Fig. 11. Pumping power vs. Inlet velocity.

ated shear layer that significantly influences the flow patterns and pathlines irregularities in the middle part. As presented in Fig. 10, there is a main difference between the pathlines of SWS and WSW models. In all SWS models, the difference of shear strain rate in the middle part is significant, resulting in large velocity gradients in the fluid zone and strengthening the secondary flow in the passage. In addition, most of the pathlines coming from each minichannel rotate 180 degrees in the middle part and then return to the adjacent minichannel. This phenomenon is more evident in SWS3 and then SWS2, which leads to more significant pressure loss values or pumping power (P_P), as depicted in Fig. 11. However, almost uniform shear rate distributions are evident in WSW models because of the straight flow patterns in the middle part. In WSW models except WSW3, most of the pathlines coming from each minichannel continue to flow in the same direction and enter the opposite minichannel. Details of the change in the flow pattern of WSW3 are described in Fig. 7. Therefore, among WSW models, this model (WSW3) offers the highest values of P_P. Regarding Fig. 11, after WSW3, WSW1 possesses higher P_P due to the produced swirl flows and pathlines irregularities in the middle part.

It can be seen that P_P has a rising trend with increasing u_{in} (Re). Depending on u_{in}, P_P in the novel minichannels is 2.6-8.03 times as large as that of the straight minichannels. The increasing of P_P with u_{in} can be justified for two reasons: (i) as u_{in} is increased, more velocity variations occur, which results in drastic shear rates inside the flow path, so the pressure loss (or P_P) increases, and (ii) at the same time, the flow features inside the wavy flow path change by increasing u_{in}. From Fig. 7, the pathlines become completely irregular with increasing u_{in}, and the features of swirl flows change and finally affect P_P. The results show the highest and lowest augmentations for SWS3 and WSW2 with average values of 4.09 and 5.91, respectively. Therefore, significant reduction in P_P can be achieved by replacing the wavy fins (SWS) with the wavy walls (WSW).

4. Overall Performance

From the results and discussion argued in the previous sections, it is obvious that the novel minichannels bring larger thermal performance and lower $T_{b,avg.}$ and $\Delta T_{b,max.}$, particularly at bigger u_{in}. However, the temperature uniformity (θ) at the base surface plays a crucial role in heat sinks performance because the base surface is in direct contact with the hot region of electromechanical systems. As a matter of fact, hotspots on these systems are the result of temperature non-uniformity, which can destroy the equipment and reduce the lifetime. The most significant point is that the temperature uniformity should occur at the lower base temperature. For instance, in WSW4, although θ at P_P=0.0024 W is approximately equal to θ at P_P=0.0374 W, $T_{b,avg.}$ at P_P=0.0024 W is about 6.75 K

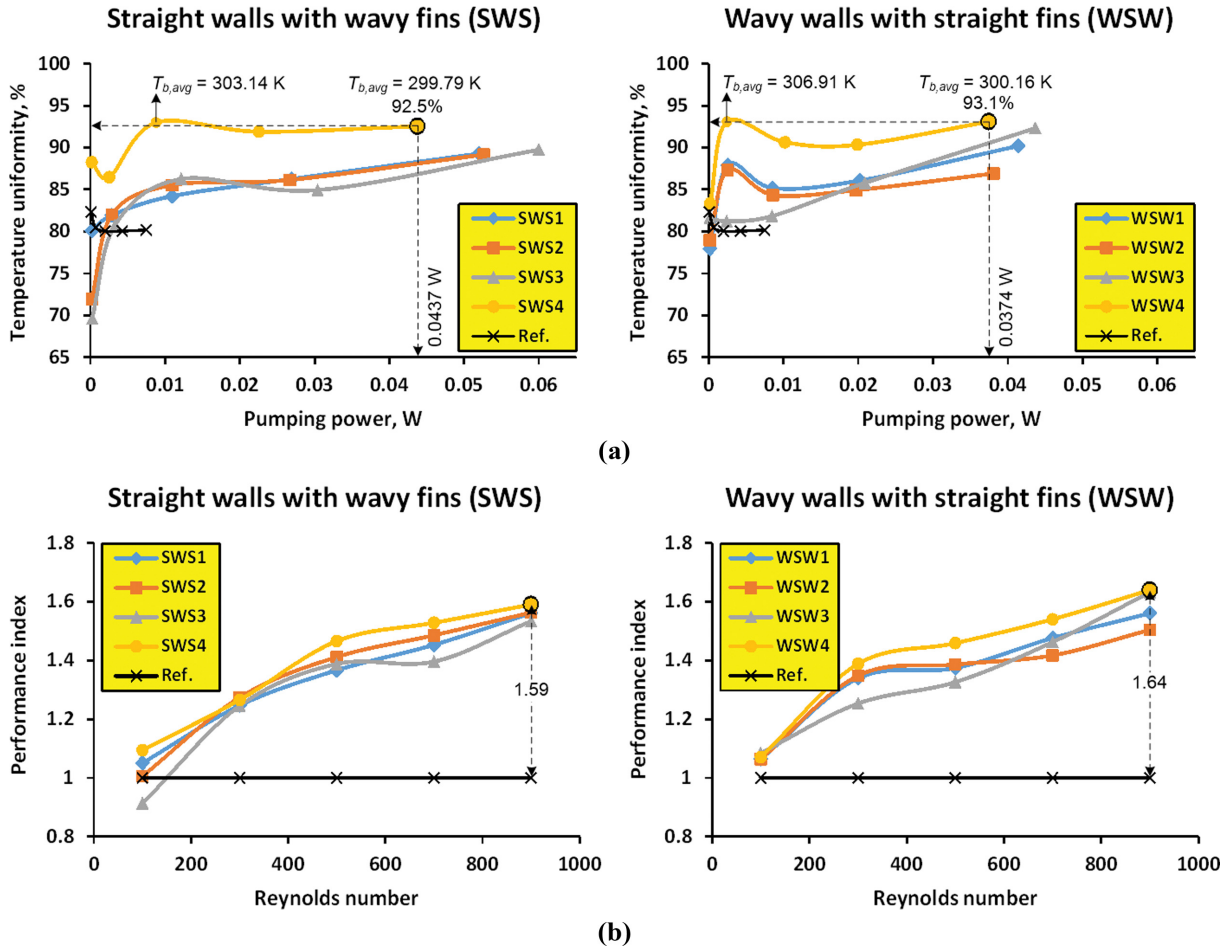
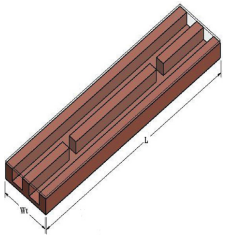
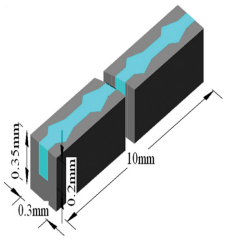
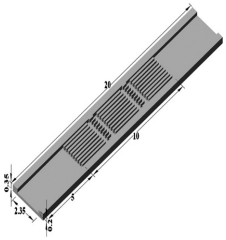
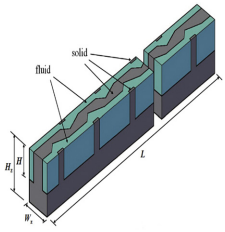
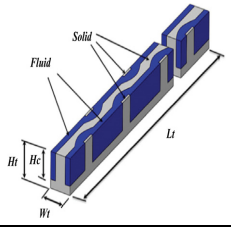
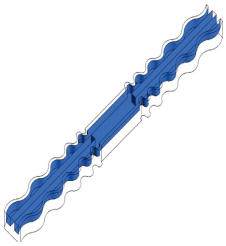


Fig. 12. (a) Temperature uniformity vs. Pumping power (b) Performance index vs. Reynolds number.

larger than $T_{b,avg.}$ at P_P=0.0374 W. This high $T_{b,avg.}$ may not be able to dissipate heat adequately from the hot surface of the equipment because of the low thermal driving force. According to temperature contours provided in Fig. 9(a), it can be perceived that utilizing SWS4 and WSW4 results in a more uniform temperature on the base surface, but to create a quantitative assessment, the alteration of θ versus P_P is plotted in Fig. 12(a). According to this figure, θ rises with increasing P_P. Moreover, utilizing SWS4 and WSW4

Table 5. Comparison of results from the literature with the present study

Reference	Type of investigation	Geometry	Augmentation method	Summary of result
Tikadara et al. [33]	Numerical		Inter-connected counter-flow	In the case of counter-flow, inter-connectors had a significant effect on the temperature profile of the heat sink with respect to parallel flow. Also, the η varied from 1.06 to 1.33, and it showed an increasing trend with Re.
Xia et al. [34]	Numerical		Triangular reentrant cavities	The size of the triangular reentrant cavity and also the ratio of the expansion/constriction segment to the constant took into consideration to optimize heat transfer. The minimum and maximum values of η were 0.96 and 1.63, respectively.
Chai et al. [35]	Experimental and Numerical		Staggered rectangular ribs	For heat transfer enhancement, the interrupted microchannel with ribs was suitable to the operating condition of Re<600, and for Re>600, the interrupted micro- channel without ribs was considered better. The range of η varied between 1.35 and 1.51.
Li et al. [36]	Numerical		Triangular cavities and rectangular ribs	The proposed microchannel heat sink exhibited more uniform and lower temperature at the substrate. Moreover, the η accounted for 1.47 at lower Re and then reached to 1.59.
Ghani et al. [37]	Numerical		Sinusoidal cavities and rectangular ribs	The smooth surface had a highest average base surface temperature followed by microchannel with cavities, ribs, and the combination of cavity and rib, respectively. The maximum and minimum value of η was 1.83 and 1.21, respectively.
Present study	Experimental and Numerical		Counter flow with wavy walls with straight fins	18.1-40.3% decrease in the base temperature with the novel structures was reported. Also, the η of WSW4 was between 1.07 and 1.64.

improves the temperature uniformity of heat sinks. The highest values of θ for these models are around 92.5% and 93.1% at P_p of 0.0437 W and 0.0374 W, respectively.

To appraise the novel minichannel performance, the alterations of the considered performance index (η) against Re are presented in Fig. 12(b). It is evident that the novel minichannels offer larger values of η compared to the conventional or straight minichannels. This can be attributed to superior thermal characteristics of the novel minichannels as well as reasonable variation in hydraulic specifications, as discussed earlier. Also, all the graphs have an increasing trend with increasing Re. At high Re, more swirl flows are formed with higher power [31,32]; therefore, the flow mixing becomes stronger, which improves the thermal performance inside the minichannels. In contrast, the coolant velocity at low Re is small, so larger convective thermal resistance appears, leading to weaker thermal performance. For instance, at Re=100, the value of η for SWS4 is 1.09, while at Re=900, the value of η for this model is 1.59. The biggest improvement in the overall performance is around 1.64 for WSW3 and WSW4 when Re is 900.

5. Comparison between the Proposed and other Techniques

Using complex channels is an effective passive technique to enhance heat transfer inside the different heat exchange devices. The existence of curvatures or turbulators along the flow path disturbs the streamlines and creates some swirl flows, leading to higher heat transfer coefficients compared to the conventional straight channels. In recent years, several complex channels were also suggested and studied to improve the thermal and overall performance of heat sinks. In this section, the performance index (η) of the best technique (WSW4) in the present study is compared to that of other recent studied ones, such as interruption in counter-flow [33], triangular reentrant cavities [34], staggered rectangular ribs [35], and combination of cavities and rectangular ribs [36,37].

Table 5 and Fig. 13 present the details of this comparison. It is obvious that in the counter-flow arrangement, the overall performance of WSW4 is better than the model studied by Tikadara et al. [33]. In the case proposed by Li et al. [36] at Re<500, the performance index is higher than that of WSWs, whereas for Re>500, WSW4 has larger η than that of Chai et al. [35]. The performance index of Ref. [34] follows the same trend as that of WSW4. However, at the minimum Re, i.e., Re=100, the model proposed by Ref. [37] has a higher performance index value, while at the maximum Re, i.e., Re=900, WSW4 provides better overall performance.

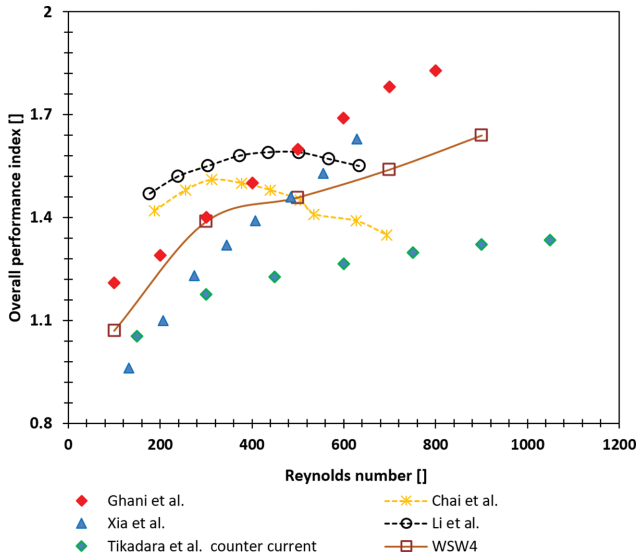


Fig. 13. Comparison of results from the literature with the current study.

CONCLUSIONS

In the current investigation, the counter-flow design complex minichannels are suggested to manage the non-uniformity of temperature on the base surface of heat sinks. A 3D numerical simulation was conducted to perform this idea and an experimental study was carried out to validate the numerical results. An excellent agreement was obtained, such that the maximum absolute deviations for Nusselt number and friction factor are 8.3% and 7.4%, respectively. The results show that the novel minichannels can offer pronounced reduction in the base temperature with certain penalties in the pumping power. It is found that by introducing the novel minichannels, the base temperature of the heat sink can be decreased about 9.64-13.34 K under the heat flux of 100 kW m^{-2}. Likewise, the maximum base temperature difference is reduced, particularly at higher coolant inlet velocities. The minimum value of 1.86 K was obtained for WSW4 at u_{in} of 0.982 m s^{-1}. Subsequently, the temperature uniformity for this model reaches 93.1% at a P_p of 0.0374 W. A further analysis illustrates that the overall hydrothermal performance of these enhanced geometries is superior to that of the straight minichannels. For example, the performance index of WSW4 is about 64% bigger than that of the conventional model at Reynolds number of 900. It can be concluded that regulating the temperature of mechanical or electronic devices, optoelectronics, high-power semiconductor devices, solar panels, and batteries is a crucial issue in reducing the damage rate of these devices, which is exponentially correlated with increasing their temperature. Excessive temperature degrades the reliability and life span of these systems. So, designing efficient heat sinks, which properly dissipate heat from these devices and provide them better temperature uniformity, is so vital.

DECLARATION OF COMPETING INTEREST

There is no conflict of interest.

NOMENCLATURE

A_c : frontal area [m^2]
A_t : wetted area [m^2]
c_p : specific heat at constant pressure [J kg^{-1} K^{-1}]
D_h : hydraulic diameter [m]
f : friction factor
h : convective heat transfer coefficient [W m^{-2} K^{-1}]
k : thermal conductivity [W m^{-1} K^{-1}]
l : minichannel length [m]
q : heat flux [W m^{-2}]
m : mass flow rate [kg s^{-1}]

Nu : Nusselt number
Re : Reynolds number
p : pressure [Pa]
P_P : pumping power [W]
T : temperature [K]
u, v : velocity [m s^{-1}]
x : span-wise
y : normal
z : stream-wise

Greek Symbols

ρ : density [kg m^{-3}]
μ : dynamic viscosity [Pa s]
η : performance index
θ : temperature uniformity

Subscripts

avg. : average
b : base
in : inlet
out : outlet
max : maximum
min : minimum
s : solid

Acronyms

SWS : straight-wavy-straight
WSW : wavy-straight-wavy

REFERENCES

1. X. Guo, Y. Fan and L. Luo, *Chem. Eng. J.*, **227**, 116 (2013).
2. H. Y. Wu and P. Cheng, *Int. J. Heat Mass Transf.*, **46**, 2547 (2003).
3. R. Roth, G. Lenk, K. Cobry and P. Woias, *Int. J. Heat Mass Transf.*, **67**, 1 (2013).
4. A. L. The, Y. W. Phoo, W. M. Chin, E. H. Ooi and J. J. Foo, *Chem. Eng. Res. Des.*, **156**, 226 (2020).
5. G. Wang, D. Niu, F. Xie, Y. Wang, X. Zhao and G. Ding, *Appl. Therm. Eng.*, **85**, 61 (2015).
6. H. E. Ahmed, *Appl. Therm. Eng.*, **102**, 1422 (2016).
7. M. Khoshvaght-Aliabadi, S. Deldar and S. M. Hassani, *Int. J. Mech. Sci.*, **148**, 442 (2018).
8. A. Sakanova, C. C. Keian and J. Zhao, *Int. J. Heat Mass Transf.*, **89**, 59 (2015).
9. M. Khoshvaght-Aliabadi, E. Ahmadian and O. Sartipzadeh, *Int. Commun. Heat Mass Transf.*, **81**, 19 (2017).
10. M. Salami, M. Khoshvaght-Aliabadi and A. Feizabadi, *J. Therm. Anal. Calorim.*, **138**, 3159 (2019).
11. J. D. Zhou, M. Hatami, D. X. Song and D. Jing, *Int. J. Heat Mass Transf.*, **103**, 715 (2016).
12. L. Chai, G. D. Xia, L. Wang, M. Zhou and Z. Cui, *Int. J. Heat Mass Transf.*, **62**, 741 (2013).
13. Y. L. Zhai, G. D. Xia, X. F. Liu and Y. F. Li, *Int. J. Heat Mass Transf.*, **84**, 293 (2015).
14. G. D. Xia, J. Jiang, J. Wang, Y. L. Zhai and D. D. Ma, *Int. J. Heat Mass Transf.*, **80**, 439 (2015).
15. C. A. Rubio-Jimenez, S. G. Kandlikar and A. Hernandez-Guerrero, *IEEE Trans. Compon. Packaging. Manuf. Technol.*, **2**, 825 (2012).
16. C. A. Rubio-Jimenez; S. G. Kandlikar and A. Hernandez-Guerrero, *IEEE Trans. Compon. Packaging. Manuf. Technol.*, **3**, 86 (2013).
17. M. Vilarrubí, S. Riera, M. Ibañez, M. Omri, G. Laguna, L. Fréchette and J. Barraua, *Int. J. Therm. Sci.*, **132**, 424 (2018).
18. S. Feng, Y. Yan, H. Li, Z. He and L. Zhang, *Int. J. Heat Mass Transf.*, **156**, 119675 (2020).
19. S. Feng, Y. Yan, H. Li, Z. Yang, L. Li and L. Zhang, *Appl. Therm. Eng.*, **153**, 748 (2019).
20. S. Feng, Y. Yan, H. Li, F. Xu and L. Zhang, *Int. J. Heat Mass Transf.*, **159**, 120118 (2020).
21. D. Lorenzini-Gutierrez and S. G. Kandlikar, *J. Electron. Packag.*, **136**, 021007 (2014).
22. J. L. Gonzalez-Hernandez, S. G. Kandlikar and A. Hernandez-Guerrero, *Heat Transf. Eng.*, **37**, 1369 (2016).
23. P. Li, D. Guo and X. Huang, *Int. J. Heat Mass Transf.*, **146**, 118846 (2020).
24. C. Leng, X. D. Wang, T. H. Wang and W. M. Yan, *Energy Convers. Manag.*, **93**, 141 (2015).
25. M. Khoshvaght-Aliabadi and F. Hormozi, *Arab. J. Sci. Eng.*, **38**, 3515 (2013).
26. M. Bahiraei, N. Mazaheri and M. R. Daneshyar, *Appl. Therm. Eng.*, **183**, 116159 (2021).
27. R. L. Webb, *Int. J. Heat Mass Transf.*, **24**, 715 (1981).
28. A. Tikadar, T. C. Paul, S. K. Oudah, N. M. Abdulrazzaq, A. S. Salman and J. A. Khan, *Int. Commun. Heat Mass Transf.*, **111**, 104447 (2020).
29. Z. Chamanroy and M. Khoshvaght-Aliabadi, *Int. J. Therm. Sci.*, **146**, 106071 (2019).
30. S. M. Hassani, M. Khoshvaght-Aliabadi and S. H. Mazloumi, *Chem. Eng. Sci.*, **191**, 436 (2018).
31. M. Khoshvaght-Aliabadi, A. Feizabadi and S. F. Khaligh, *Int. J. Mech. Sci.*, **157**, 25 (2019).
32. M. Khoshvaght-Aliabadi and A. Feizabadi, *Sol Energy*, **199**, 552 (2020).
33. A. Tikadar, S. K. Oudah, T. C. Paul, A. S. Salman, A. K. M. M. Morshed and J. A. Khan, *Appl. Therm. Eng.*, **153**, 15 (2019).
34. G. Xia, L. Chai, H. Wang, M. Zhou and Z. Cui, *Appl. Therm. Eng.*, **31**, 1208 (2011).
35. L. Chai, G. Xia, M. Zhou, J. Li and J. Qi, *Appl. Therm. Eng.*, **51**, 880 (2013).
36. Y. F. Li, G. D. Xia, D. D. Ma, Y. T. Jia and J. Wang, *Int. J. Heat Mass Transf.*, **98**, 17 (2016).
37. I. A. Ghani, N. Kamaruzaman and N. A. C. Sidik, *Int. J. Heat Mass Transf.*, **108**, 1969 (2017).